Int. J. Electrochem. Sci., 14 **(2019)** 8340 – 8354, doi: 10.20964/2019.08.85

International Journal of
ELECTROCHEMICAL
SCIENCE
www.electrochemsci.org

The REV-scale Lattice Boltzmann Method Numerical Simulation of Flow and Mass Transfer in Porous Electrode Plate of Zinc-nickel single-flow battery

Yao Shouguang[1,*], *Wu Hao*[1], *Xiao Min*[1], *Cheng Jie*[2], *Shen Yaju*[2]

[1]Jiangsu University of Science and Technology, Zhenjiang 212003, China
[2] Zhangjiagang Zhidian Fanghua Storage Research Institute, Zhangjiagang 215600, China
[*]E-mail: zjyaosg@126.com

Received: 1 April 2019 / *Accepted:* 21 May 2019 / *Published:* 30 June 2019

Based on the lattice Boltzmann method, the flow mass transfer process of the electrolyte in the porous cathode of zinc-nickel single-liquid battery in the entire percolation region was numerically simulated from the characterization of the voxel (REV) scale. Firstly, based on the cell structure and the structure characteristics of the battery sintered nickel porous medium, a 2D porous region calculation model is constructed. The average physical quantity of the porous medium is defined by the volume average method on the REV scale, and the LBE model based on the general seepage model is selected. A computational analysis model was established. On this basis, the numerical simulation of the flow mass transfer process inside and on the porous electrode was performed. The change of velocity field and concentration field distribution in the electrode channel of the battery were obtained. Increasing the inlet flow rate of the electrolyte was beneficial to the increase of the percolation intensity in the porous medium. Finally, the percolation velocity was increased. At the same time, the charging density was appropriately increased. Thus, the reaction rate in the electrode was accelerated, and the ion concentration finally reached a stable value. The influence of electrolyte flow rate and constant current charging current density on the electrode reaction in the flow channel needs further exploration.

Keywords: Lattice Boltzmann method, REV scale, Porous medium seepage, flow mass transfer

1. INTRODUCTION

With the discovery of renewable and clean energies, such as solar and wind, it is urgent to develop large-scale energy storage devices. The flow battery generally has the characteristics of long life, high efficiency, and independent design of power and capacity. It has become a chemical energy storage technology suitable for large-scale energy storage [1-3]. As a newly developed single-flow

battery, the zinc-nickel single-flow battery has the main advantage of having no ion exchange membrane compared with the conventional two-flow battery, thereby leading to a simple battery structure and reduction of cross-contamination. In the early stage, the studies on zinc-nickel single-flow batteries were mainly based on experimental research [4-5], mainly for macroscopic numerical simulation of battery stack. In [6], the 3D mathematical model of the flow field analysis of zinc-nickel single-liquid battery stack was established. The influence of the inlet flow channel on the flow uniformity in different directions inside the stack was analyzed. Then, by establishing a 3D steady-state model of flow mass transfer and electrochemical reaction between plates of zinc-nickel single-flow battery cells, the 3D distribution of ion concentration and current density in the battery are analyzed [7]. Furthermore, the 3D steady-state thermal analysis model of zinc-nickel single-liquid battery was established, and the distribution of internal temperature field of the battery was studied [8]. Seepage and mass transfer inside the porous electrode of zinc-nickel single-flow battery are typical multi-scale problems. At present, the research on the flow and mass transfer in porous media based on LBM scale shows unique advantages [9-10]. Liao [11] used the REV-scale dual-distribution function model to simulate the biological reaction process in porous media in biofuel cells, and obtained the concentration field and flow field of hydrogen and glucose solution. Chen Rou [12] used LBM to simulate the multi-component mass transfer process in PEMFC, and obtained hydrogen, oxygen concentration distribution, potential distribution map, and volt-ampere characteristic curve of the battery. Xu [13] established a coupled LB model of 2D multi-component flow and REV-scale porous media flow based on two-fluid model. The model is used to obtain multi-component reaction gas in porous anode and cathode of solid oxide fuel cell. The internal mass transfer process was simulated, and the mole fraction distribution of each component inside the electrode was calculated. The concentration polarization was predicted based on this. Xu [14] established an REV model to analyze the electrochemical properties in porous electrodes of solid oxide fuel cells, the effects of the structure, operating temperature, and fuel composition of the porous electrode on the volt-ampere characteristics and concentration polarization of the solid oxide fuel cell were investigated.

In this paper, a 2D calculation region model of porous cathode in a unit electrode is established to determine the structural characteristics of a porous electrode of a zinc-nickel single-flow battery. According to the structural characteristics of sintered nickel, a porous medium model was constructed by computer [15-16]. On this basis, the lattice Boltzmann method is used to simulate the flow and mass transfer in the seepage region of the observation area on the REV scale. The process of seepage and mass transfer inside the porous electrode under different inlet flow rates, porosities and charging current densities were investigated. Results of this study would lay the foundation for further research [17].

2. ESTABLISHMENT OF REV SCALE LBM CALCULATION MODEL

2.1. Computational physical model

Considering that the positive and negative surfaces of the battery are porous media, and the interface between the porous medium and the mainstream channel is almost equivalent to no slip boundary, the electrolyte mainstream channel can be approximated as symmetrical according to the structural characteristics of the zinc-nickel single-flow battery stack [18]. The porous positive electrode

calculation region in the unit electrode is simplified to the 2D calculation region shown in FIG. 1. The upper portion is the electrolyte flow channel, and the width is equal to half of the complete channel. The lower portion of the porous electrode is the thickness of the complete positive electrode. B1 is the inlet of the flow channel. B2 is the boundary of the porous electrode at the inlet end, where it had no material exchange with the outside, i.e., the closed surface. B3 is the collector side of the porous positive electrode, which is the closed surface. B4 is the outlet of the porous electrode. The cross section, which also neglects the mass exchange with the porous electrode outside the region, is regarded as the closed surface. B5 is the outlet cross section of the main flow channel of the electrolyte, where the flow channel outlet of the calculation region is located. B6 is the center line of the complete electrolyte flow channel. L_1、L_2、and L_3、indicate the calculated area width, calculated area length, and porous medium area width (electrode thickness), and the respective values are 1600 μm, 2400 μm, and 400 μm.

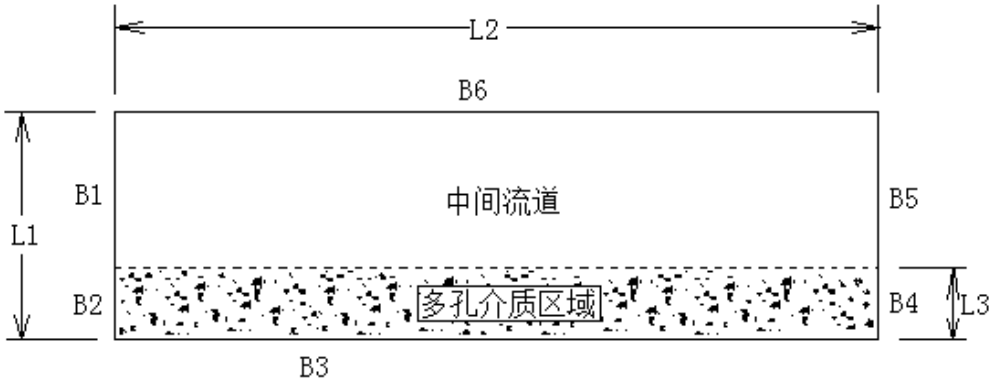

Figure 1. Schematic diagram of calculation area of zinc-nickel single-flow porous electrode

2.2. Porous flow lattice Boltzmann model

When simulating the flow of fluid in a porous medium, Nithiarasu [19] proposed a general percolation model based on the isothermal flow of an incompressible fluid in a porous medium. This model not only included linearity (Darcy) but also the nonlinear (Forchheimer) medium resistance term.The governing equation for the flow of porous media was as follows:

$$\nabla \cdot \mathrm{u} = 0 \tag{1}$$

$$\frac{\partial \mathrm{u}}{\partial \mathrm{t}} + (\mathrm{u} \cdot \nabla)\left[\frac{u}{\varepsilon}\right] = -\frac{1}{\rho}\nabla(\varepsilon p) + \upsilon_e \nabla^2 u + F \tag{2}$$

where ρ is the fluid density. u and P represent the macroscopic velocity and pressure. $\upsilon_e = \mu_e / \rho$ is the effective kinematic viscosity coefficient. F is the total force including the medium resistance and the external force, as follows:

$$F = -\frac{\varepsilon \nu}{K} u - \frac{\varepsilon F_\varepsilon}{\sqrt{K}} |u| u + \varepsilon G \tag{3}$$

where υ is the kinematic viscosity coefficient, $-\frac{\varepsilon\nu}{K}u$ and $-\frac{\varepsilon F_\varepsilon}{\sqrt{K}}|u|u$ are linear (Darcy) and nonlinear (Forchheimer) dielectric resistance respectively , and G is external volume force. The structural coefficient F_ε, and the permeability K are related to the porosity ε. For the solid particle-laden porous medium, the form is $F_\varepsilon = \frac{1.75}{\sqrt{150\varepsilon^3}}$, $K = \frac{\varepsilon^2 d_p^2}{150(1-\varepsilon)^2}$, where d_p is the diameter of the solid particles.

The following calculations are made for the calculation area of a single porous electrode. (i) Regardless of the heat generated by the chemical reaction, the physical properties of the electrolyte, such as density and viscosity, are regarded as constants in the numerical calculation, and the values are obtained at a certain reference temperature value. (ii) Calculations are irrespective of electrode side reactions and their effects. (iii) Porous dielectric materials are rigid, uniform, isotropic, and filled with electrolytes and are incompressible fluids; the flow is laminar.

2.3. Model of generalized N-S equation

In the framework of the porous flow LBM model, the single relaxation (BGK) model is used in this paper. With the D2Q9 lattice discrete velocity, the evolution equation of the distribution function is as follows:

$$f_i(x+\Delta x, t+\Delta t) - f_i(x,t) = -\omega[f_i(x,t) - f_i^{eq}(x,t)] + \delta_t F_i \quad (4)$$

In the form, f_i is a particle distribution function with an i-direction velocity at x at time t. Δt is the time step, $\omega = \frac{\Delta t}{\tau}$ represents the relaxation frequency. τ is called the relaxation factor. The relationship between the fluid viscosity ν and the relaxation frequency ω is $\nu = \frac{\Delta x^2}{3\Delta t}(\omega - 0.5)$, where Δx is the length of the lattice, $\Delta x = c_i \Delta t$, and c_i is the discrete velocity of particles along discrete directions. Using the D2Q9 model, the equilibrium distribution function is as follows:

$$f_i^{eq} = w_i \rho[1 + \frac{c_k \cdot u}{c_s^2} + \frac{(c_k \cdot u)^2}{2c_s^4} + \frac{u \cdot u}{2c_s^2}] \quad (5)$$

$$F_i = \rho\omega_i\left(1 - \frac{1}{2\tau}\right)\left[\frac{e_i \cdot F}{c_S^2} + \frac{(e_i \cdot u)\cdot(e_i \cdot F)}{\varepsilon c_S^4} - \frac{u \cdot F}{\varepsilon c_S^2}\right] \quad (6)$$

In the form, ρ indicates fluid density（kg/m^3）, $c_s = \frac{c_k}{\sqrt{3}}; c_k = \frac{\Delta x}{\Delta t}\vec{i} + \frac{\Delta y}{\Delta t}\vec{j}$; w_i represents the weighting factor, as follows: $i = 0, w_i = 4/9; i = 1 \sim 4, w_i = 1/9$; and $i = 5 \sim 8, w_i = 1/36$. The migration direction and weighting factors are shown in Figure 2. F_i is the distribution function of the external force term. The total force F is determined by the equation. Porosity ε is included in f_i^{eq} and F_i.

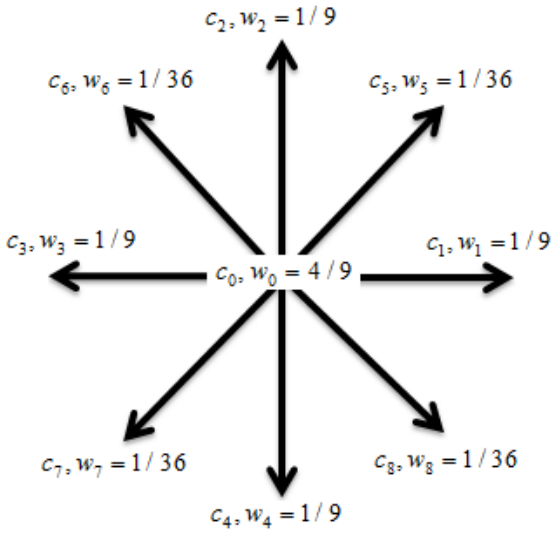

Figure 2. Migration direction and weighting factor

Seepage density and velocity are defined as follows:

$$\rho=\sum_i f_i \,,\ \rho u = \sum_i \left(e_i \cdot f_i + \frac{\delta_t}{2} \rho F \right) \tag{7}$$

F contains flow velocity u. Therefore, the equation is a two-order nonlinear equation of velocity, which is directly solved as follows:

$$u = \frac{v}{c_0 + \sqrt{c_0^2 + c_1 |v|}} \tag{8}$$

The temporary speed v is as follows:

$$\rho v = \sum \left(e_i \cdot f_i + \frac{\delta_t}{2} \varepsilon \rho G \right) \tag{9}$$

Parameters c_0 and c_1 are the following:

$$c_0 = \frac{1}{2}\left(1 + \varepsilon \frac{\delta_t}{2} \frac{v}{K}\right),\ \ c_1 = \varepsilon \frac{\delta_t}{2} \frac{F_\varepsilon}{\sqrt{K}} \tag{10}$$

The equilibrium distribution function of the model contains the porosity of the reaction medium characteristics, whereas the equilibrium distribution function of the remaining REV-scale LBE [20-21]. model is similar to the standard model and does not reflect the dielectric properties. The REV-scale LBE method is no longer concerned with the flow details within the pores. Its purpose is to obtain a volume-averaged macro flow situation. The REV-LBE model also does not require the specific pore structure of the porous medium. However, the statistical properties of the medium, such as porosity permeability, are required. These data can be obtained from experimental or theoretical models and can be used for calculation of large-scale seepage fields.

When calculating in grid units, the physical unit needs to be converted to the grid unit. Taking the D2Q9 model as an example, the basic lattice unit parameters in the simulation are length L, density ρ, time t, and kinematic viscosity coefficient υ. The corresponding physical unit parameters are length L', density ρ', time t', and kinematic viscosity coefficient υ'. The conversion between the two units

requires a reference amount, definition of the reference length, $L_r = \frac{L'}{L}$; reference density, $\rho_r = \frac{\rho'}{\rho}$; reference speed, $u_r = \frac{C_s'}{C_s}$; time conversion relationship, $\frac{L_r}{u_r} = \frac{t'}{t}$; and viscous transformation relationship, $L_r u_r = \frac{\upsilon'}{\upsilon}$.

3. POSITIVE MASS TRANSFER AND REACTION MODEL

In the zinc-nickel single-flow battery system, the positive and negative electrodes of the battery are immersed in the $K_2Zn(OH)_4$-KOH solution, and the nickel oxide electrode is a porous material. The mass transfer process in the electrode includes solid phase proton transfer and hydroxide ion transport in the liquid phase. The reaction is mainly a redox reaction between $Ni(OH)_2$ and NiOOH on the surface of the solid phase [22].

3.1. Positive electrode reaction process and reaction rate equation

During the charging and discharging of the positive electrode, the chemical equation of the reaction is as follows:

$$2NiOOH+2H_2O+2e^- \underset{charge}{\overset{discharge}{\rightleftharpoons}} 2Ni(OH)_2 + 2OH^- \quad (11)$$

Positive reaction rate equation is as follows:

$$j_{Ni} = i_{Ni,ref}\left(\frac{c^{OH}}{c_{ref}^{OH}}\right)^{(1-\alpha_1)}\left(\frac{c^{H}}{c_{ref}^{H}}\right)^{(1-\alpha_1)}\left(\frac{c_{\max}^{H}-c^{H}}{c_{\max}^{H}-c_{ref}^{H}}\right)^{\alpha_{\alpha 1}}\left[\exp\left(\frac{\alpha_1 F}{RT}\eta_1\right)-\exp\left(-\frac{(1-\alpha_1)F}{RT}\eta_1\right)\right] \quad (12)$$

3.2. Mass transfer LBM model

For the mass transfer process, the mass transfer model of the lattice Boltzmann method is needed for calculation. To simplify the calculation, it is assumed that the mass transfer process does not affect the flow of the fluid, that is, the flow and mass transfer processes are not coupled for calculation, and the velocity appears in the mass transfer model. The term is a known quantity. The area model is calculated as stated in the previous section, and the obtained velocity field is brought into the mass transfer equation of this section for calculation. The concentration distribution is calculated according to the flow field. For mass transfer processes with chemical reactions, the lattice Boltzmann mass transfer model uses a single relaxation model, and the general form of the lattice BGK equation is as follows:

$$g_i(x+\Delta x, t+\Delta t) = g_i(x,t)[1-\omega] + \omega g_i^{eq}(x,t) + S \quad (13)$$

Among them, the balance distribution function is as follows:

$$g_i^{eq} = w_i\phi(x,t)\left[1+\frac{c_k \cdot \vec{u}}{c_s^{\,2}}\right] \quad (14)$$

where S_E is the external force term and the electromigration source term, as follows:

$$S_E = w_i \phi(x,t) \frac{c_k}{c_s^2} \cdot \frac{zF\vec{E}}{RT} \left(\Delta t \Delta x^2 \right) \quad (15)$$

where F is a Ferrari (C/mol), $\vec{E}$ is the electric field strength (V/m), and Δt and Δx are time scales and spatial scales.

The mass transfer process still uses the D2Q9 model to discretize the velocity. Thus, the parameters in the above equations are similar to the flow model and are not described in detail.

Based on the above mentioned calculation model, this paper simulates the flow and mass transfer process in the calculation area by changing the following conditions: 1) the inlet velocity of the B1 boundary; 2) the porosity of the porous medium; and 3) the charging current density.

4. SIMULATION RESULTS AND DISCUSSION

4.1. Distribution pattern of whole flow field velocity cloud map and distribution of seepage velocity field

The figure below is the calculation area. The number of grids used is 2400×1600. The inlet flow rate is 0.006 m/s. The inlet flow rate of the single channel of the battery is calculated by the experimental flow conversion of zinc-nickel single-flow battery. The flow channel width ($d/2 = 1.6mm$). Porosity of porous media on the surface of nickel oxide cathode ($\varepsilon = 0.45$). The whole field velocity distribution obtained is shown in Fig. 3.

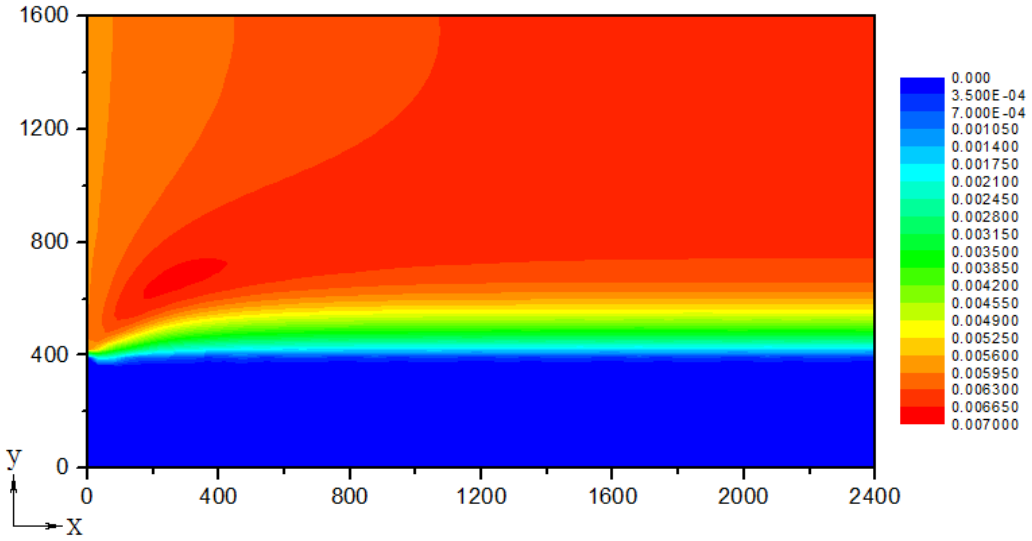

Figure 3. Whole-field velocity cloud

The velocity map of the whole field showed that the fluid velocity inside the porous medium is close to 0 when compared with the fluid velocity in the flow channel, but it is less than 0. The overall

percolation velocity inside the porous medium is several orders of magnitude different from the fluid velocity in the flow channel. The electrolyte in the flow path initially undergoes a development zone at the inlet, after which the electrolyte flow rate is continuously increased and then enters the fully developed section. The final velocity reaches a stable value.

4.2. Comparison of pore scale LBM simulation and REV scale

The LBM computational physical model of the pore-scale flow mass transfer process is basically the same as the computational physical model in 1.1. The difference is mainly reflected in two points: (i) The size of the calculation area under the pore scale is small, L_1、L_2、and L_3 indicate the calculated area width, calculated area length, and porous medium area width (electrode thickness), and the values are 100, 400, 30 grid units, and the actual length of a single grid length in the calculation area is 1 micron. (ii) The structure of the porous medium region at the pore scale, the volume expansion ratio of the positive electrode of the zinc-nickel single-liquid battery is 1% to 3% under full charge and discharge state, Therefore, the microstructure changes of the internal skeleton are not considered. According to the structural characteristics of the sintered nickel electrode, a digital model of the porous electrode is constructed. The constructed porous medium digital model is introduced into the porous medium region as shown in Fig. 4 [23-24].

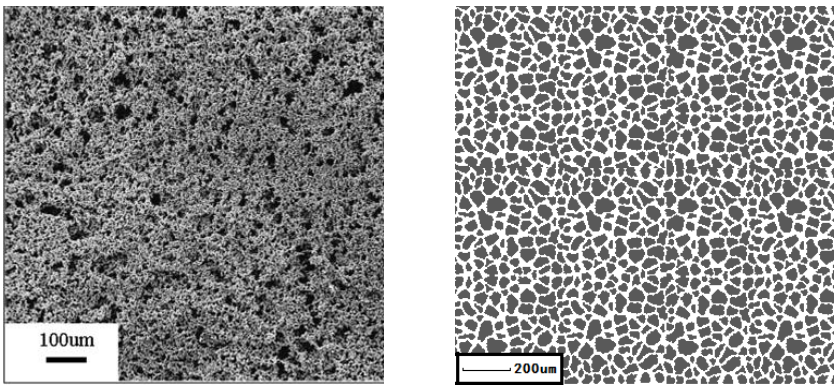

Figure 4. (a) SEM scan of sintered nickel electrode (b) Digitally reconstructed sintered nickel model

Fig. 5(a) shows the velocity distribution of the calculated area of the zinc-nickel single-liquid battery at the pore scale. Fig. 5(b) shows the velocity distribution of the percolation area inside the porous medium at the pore scale. The number of grids used is 400×100. The inlet flow rate is 0.02 m/s. Porous media calculation area size is 20×20. Compared with the flow of the zinc-nickel single-flow battery under the REV scale, the REV can take a larger calculation area and divide the large porous medium seepage area.

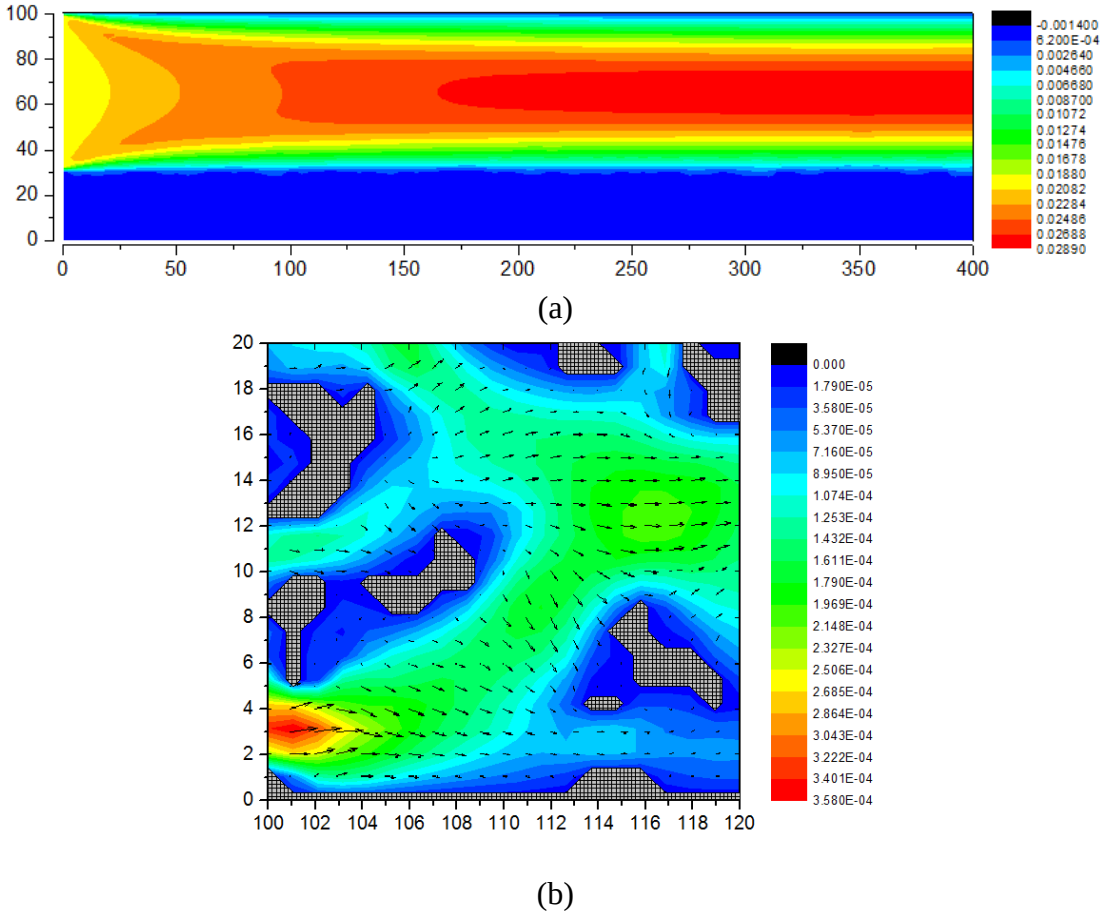

Figure 5. (a) Calculating the velocity distribution of the region (b) Seeking the internal porous media

Fig. 3 and Fig. 5 show the velocity field distribution over the entire calculation area at the REV scale and the pore scale. The REV scale of the calculation area is larger than the pore size, but the distribution of the overall velocity of the calculation area is basically the same. The flow velocity of the main flow channel is much larger than the flow velocity of the seepage region, and the flow velocity of the main flow channel is continuously increased, and finally stabilizes. At the REV scale, the flow velocity of the upper boundary of the main channel is basically constant in the inlet section and the fully developed section, and the flow velocity of each section is increasing. The upper boundary velocity of the main channel on the pore scale remains substantially constant in each segment and is smaller than the flow velocity in the middle of the main channel [25].

4.3 Influence of electrolyte inlet flow rate on average percolation velocity in the flow channel

Fig. 6 and Fig. 7 show the average seepage velocity along the X （$1200\mu m$—$1600\mu m$） and Y （$0\mu m-400\mu m$） directions for the inlet velocity of the runners of 0.004, 0.006, and 0.008 m/s.

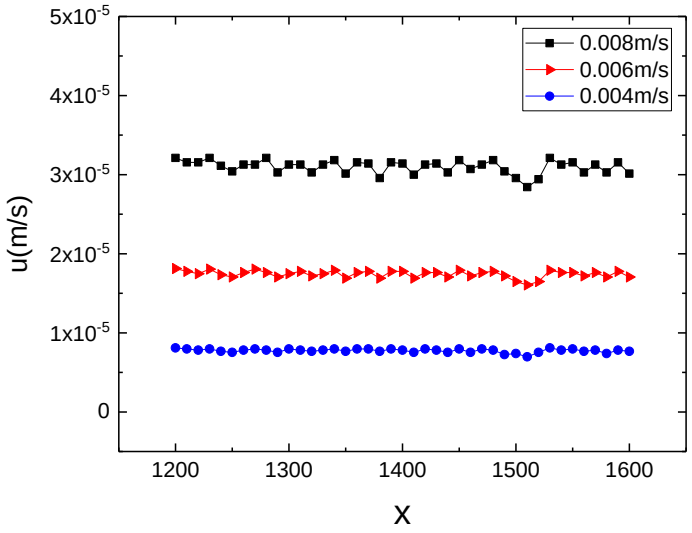

Figure 6. Distribution of average percolation velocity along the X direction at different inlet flow rates

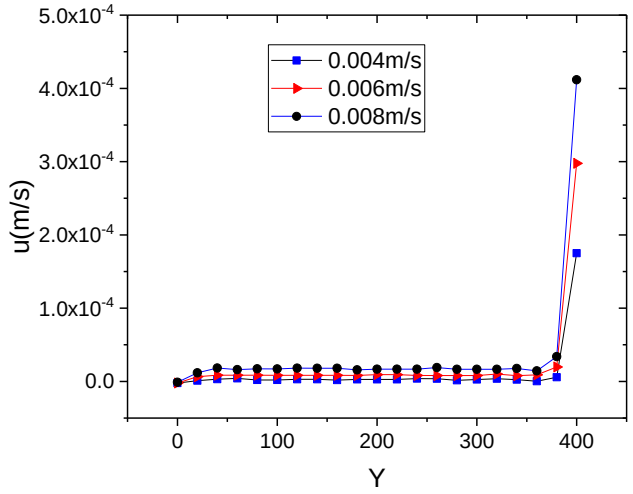

Figure 7. Distribution of average seepage velocity along the Y direction at different inlet flow rates

With increasing inlet flow rate, the average percolation velocity of the entire seepage region along the X direction significantly increased, whereas the average percolation velocity in the Y direction showed less change. The average percolation velocity remained constant at the three inlet flow rates in the range of ($0\mu m$—$380\mu m$), and the average percolation velocity increased exponentially when it reached the range of ($380\mu m$—$400\mu m$).

4.4. Effect of porosity on average seepage velocity

Fig. 8 and Fig. 9, show the inlet flow rate 0.006m/s and flow path width d/2=1.2mm. Consider the variation of the average seepage velocity along the X ($1200\mu m-1600\mu m$) and Y ($450\mu m-700\mu m$) directions in the porous medium at porosity values of 0.55, 0.45, and 0.35.

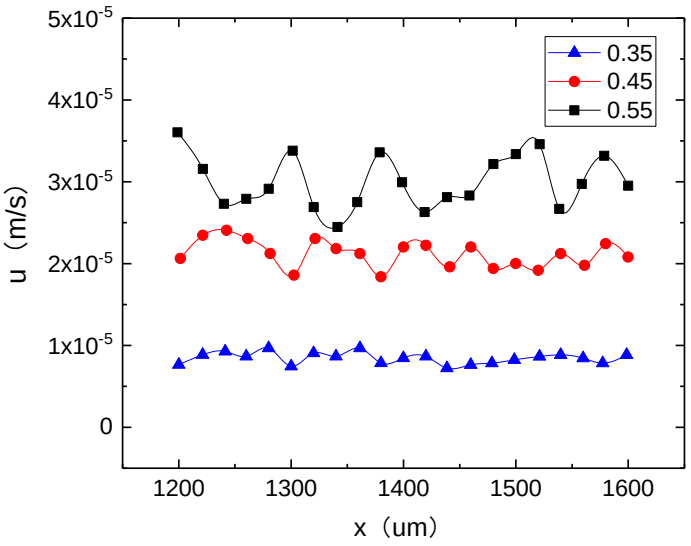

Figure 8. Average percolation velocity along the X direction in a porous medium corresponding to different porosity values

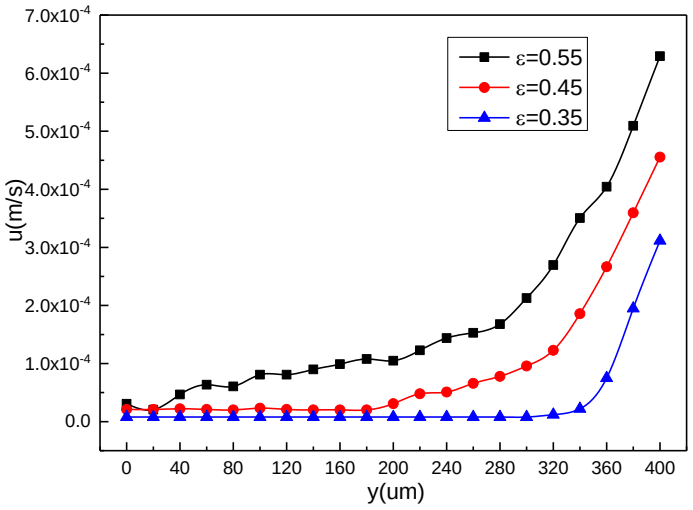

Figure 9. Average percolation velocity along the Y direction in a porous medium corresponding to different porosity values

The percolation velocity of the electrolyte in the X and Y directions increase in the porous medium with increasing porosity. Moreover, the average percolation velocity in the X direction increases while fluctuating with increasing porosity. The amplitude also increases. The average percolation velocity in the Y direction in the pores begins to decrease faster and then stabilizes. The Darcy formula shows that with increasing porosity, the permeability increases. In the momentum equation, the Brinkman resistance represents the viscous resistance of the porous skeleton to the fluid, whereas the Forchheimer inertial resistance is proportional to the square of the fluid velocity. In the laminar flow zone, Brinkman resistance is much greater than Forchheimer inertial resistance. With increasing porosity

of the porous medium, the specific surface area of the porous medium decreases, the viscous resistance of the porous skeleton to the fluid decreases, and the Brinkman resistance decreases much more than the increase in Forchheimer inertial resistance [26]. The porosity of the porous medium is effectively improved. The flow resistance is reduced. With increasing porosity, the percolation rate of the electrolyte in the porous medium increases.

4.5. Liquid phase OH^- ion concentration distribution

First, the distribution of electrolyte concentration in the electrolyte flow channel and the electrode during the charging process is analyzed. The set inlet speed is 0.006m/s, and the charging current density is $15\,mA/cm^2$. The simulation shows the concentration cloud in the entire calculation area (Fig. 10).

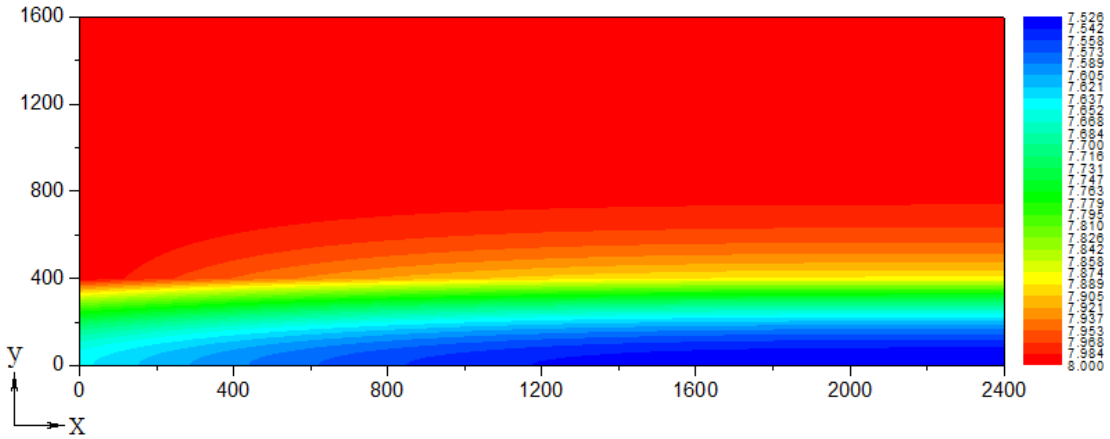

Figure 10. Calculation area OH^- concentration cloud map

From the simulation results, the OH^- concentration distribution in the whole flow channel is relatively uniform, and the OH^- concentration in the main flow region is basically unchanged in the X and Y directions. In the vicinity of the electrode surface, the ion concentration decreases significantly in the direction of the vertical flow channel and in the flow channel direction. The electrode surface and the internal ion concentration of the electrode are slightly reduced. Under the given simulation conditions, the mass transfer process in the electrode is far less than the reaction in the flow channel area. Thus, the relative difference in ion concentration is larger.

4.6. Effect of charging current density on liquid phase OH^- ion concentration

During constant charging of the battery, the charging current density is given; it determines the total rate of chemical reactions in the entire simulated region. During charging, the consumption rate of liquid phase OH- and solid phase protons increases with increasing charging current density. The transport rate of liquid phase OH- and solid phase protons to the surface of the solid phase framework increases. Thus, the liquid phase OH- concentration distribution and solid phase proton distribution are significantly affected. Fig. 11 shows the average concentration of the electrode near the flow channel

measured in the X ($0\mu m - 2400\mu m$) direction at charging current densities of 5.0, 10, 15, and 20 mA/cm^2.

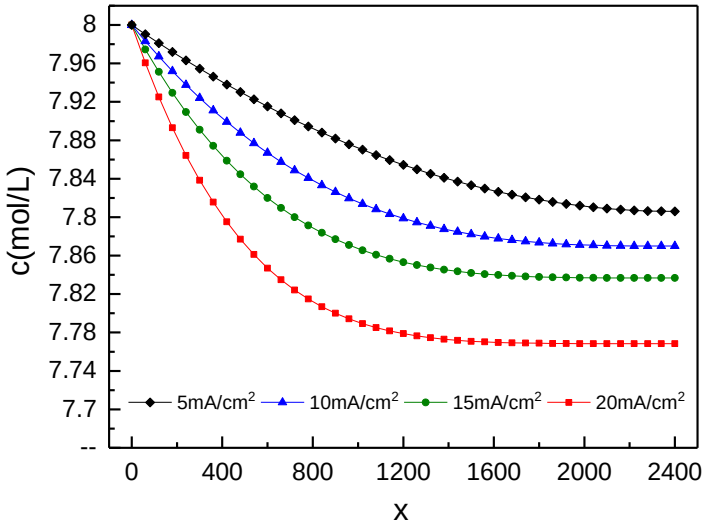

Figure 11. OH- ion concentration on the surface of the electrode at different charge current densities distributed along the x direction

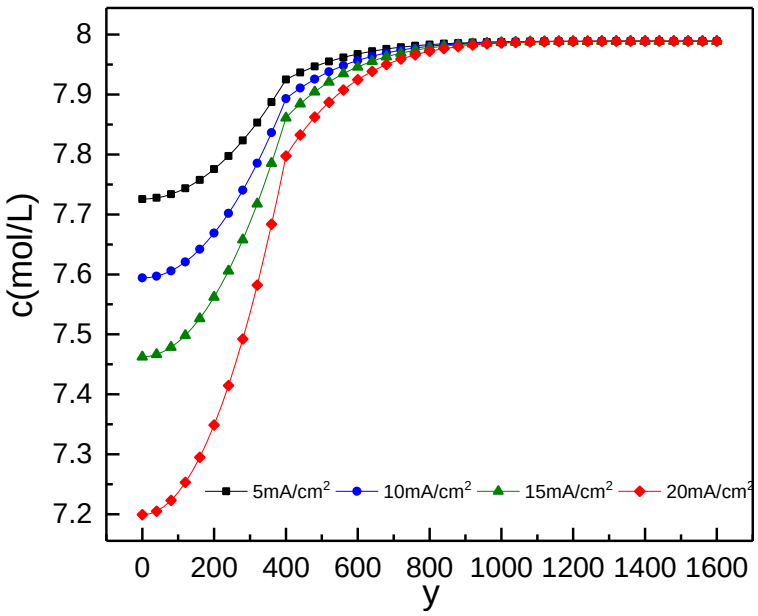

Figure 12. OH^- ion concentration on the surface of the electrode at different charge current densities distributed along the y direction

The charging current density has a significant influence on the concentration measured by the near flow channel of the electrode [27]. At high charging current density, ion concentration takes longer to reach a relatively stable distance, and the length of the development zone increases. As the charging current density increases, the stable value of the ion concentration decreases correspondingly. However,

as the charging current density further increases, the decreasing value of the stable value of the ion concentration increases [28].

Fig. 12 shows the distribution of the average ion concentration in the Y ($0\mu m - 1600\mu m$) direction at X=1200, and the charging current densities are 5.0, 10, 15, and 20 mA/cm^2.

The variation of the charging current density setting value affects the overall concentration distribution of the OH^- inside the electrode surface and the electrode. As the charging current density increases, the electrode near-flow path measurement and the internal ion concentration of the electrode correspondingly decrease, and the electrode far-flow measurement ion concentration reduction value is large.

5. CONCLUSION

For the zinc-nickel single-flow battery, the REV-scale flow mass transfer and chemical reaction analysis model of the positive electrode in the unit electrode is given. The velocity distribution of the whole flow field and the liquid-phase OH^- ion concentration distribution in the whole calculation area are simulated by the lattice Boltzmann method. The effects of inlet flow rate and porosity on the distribution of seepage velocity, as well as the influence of charging current density on the concentration distribution of liquid phase OH^- ions in the calculation region are discussed.

The flow of electrolyte in the flow channel and the percolation process in the porous electrode are in two parts, namely, the electrolyte flow path and the inside of the electrode. According to the obtained whole field velocity cloud map and the whole field OH^- ion concentration distribution, the flow velocity in the flow channel is much larger than the flow velocity inside the porous medium. Speed differences result in much better overall mass transfer condition compared with the internal electrode. Thus, the electrode ion concentration measured by the near flow channel is much smaller than that of the mainstream region.

With increasing inlet flow rate, the difference in the pressure drop along the opening interface increases, and the porous medium seepage strength increases. Finally, the percolation velocity increases. At constant electrolyte flow rate and charging average current density, with increasing porosity, the volatility that affects the average percolation velocity in the X direction within the pore increases. In the Y direction, a tendency to rapidly fall and then stabilize is observed. With increase in charging current density, there is a greater decrease of the stable value of the ion concentration along the X direction. The electrode near the Y direction near-flow path and the ion concentration correspondingly decrease.

ACKNOWLEDGMENT
This work was funded by the National Natural Science Foundation of China (No. 51776092).

References

1. Y. Wen, J. Cheng, S. Ning and Y. Yang, *J. Power Sources,* 188 (2009) 301.
2. Z. Yuan, H. Zhang and X. Li, *Chem. Commun.,* 54 (2018) 7570.
3. D. Du, Q. Zhou, P. Zhao, Y. Wen and Y. Yang, *Chem Ind Eng Prog,* 32 (2013) 313.
4. J. Cheng, L. Zhang and Y. Yang, *Electrochem. commun.,* 9 (2007) 2639.

5. L. Zhang, J. Cheng and Y. Yang, *J. Power. Sources.,* 179 (2008) 381.
6. M. Xiao, Y. Wang, S. Yao, Y. Song, J. Cheng and K. He, *J. Ren. Sustainable Eng,* 8 (2016) 064102
7. S. Yao, Y. Ji, Y. Wang, Y. Song, M. Xiao and J. Cheng, *Oxid. Commun.,* 39 (2016) 3223.
8. S. Yao, M. Xiao, P. Liao, Y Song and J. Cheng, *Asian Conference. Thermal Sci,* Jeju, Korea, 2017.
9. X. Zhang and Y. Yong, *Prog Chem Ind,* 35 (2016) 1698.
10. Long. Xie, Y. Wang and J. Yu, *Power Supply Technol,* 37 (2013) 2.
11. Q. Liao, Y. Yang, X. Zhu and R. Chen, *Int. J. Hydrogen. Energ.,* 38 (2013) 15700.
12. R. Chen, S. Shao, Y. Zheng and Y. Xu, *Commun. Theor. Phys.,* 59 (2013) 370.
13. H. Xu, Z. Dang and B. Bai, *J. Fuel Cell Sci Technol,* 9 (2012) 061004.
14. H. Xu, Z. Dang and B. Bai, *Energy.,* 67 (2014) 575.
15. S. Yao, Y. Zhao, X. Sun, Q. Zhao and J. Cheng, *Electrochim. Acta.,* 307 (2019) 573.
16. S. Youcef, B.M. Hocine and Z. Bariza, *Int. J. Hydrogen Engery,* 2018.
17. C. Lin, J.D. Miller and C. Garcia, *Miner. Eng.,* 18 (2005) 1045.
18. S. Yao, Y. Li, L. Xu and J. Cheng, *Energy Procedia,* 158 (2019) 4998.
19. P. Nithiarasu, K. Seetharamu and T. Sundararajan, *Int. J. Heat. Mass. Tran.,* 40 (1997) 3955.
20. Z. Guo and T. Zhao, *Phys. Rev. E,* 66 (2002) 036304.
21. Z. Guo and T. Zhao, *Number. Heat. Tran. B.,* 47 (2005) 157.
22. S. Yao, P. Liao, M. Xiao, J. Cheng and W. Cai, *Energies.,* 10 (2017) 1101.
23. L. Liu, J. Yao, L. Zhang, S. An and J. Zhao, *J. Nat. Gas. Sci. Eng.,* (2017) 100
24. Z. Tian, H. Xing, Y. Tan and J. Gao, *Physica. A.,* (2014) 155.
25. J. Zhao, D. Fu, Y. Li, Y. Jiang and W. Xu, *J. Nat. Gas Sci. Eng.,* (2018) 224.
26. Z. Guo, C. Zheng and B. Shi, *Prog. Comput Fluid Dynam.,* 9 (2009) 225.
27. X. Guo, *J. Am. Ceram. Soc.,* 90 (2007) 2868.
28. W. Wu, Z. Liu, S. Hu, X. Li and C. Du, *Ocean. Eng,* 146 (2017) 311.